Acoustic resonance for contactless ultrasonic cavitation in alloy melts

C.E.H. Tonry[a,*], G. Djambazov[a], A. Dybalska[b], W.D. Griffiths[b], C. Beckwith[a], V. Bojarevics[a], K.A. Pericleous[a]

[a] Computational Science and Engineering Group, University of Greenwich, Park Row, Greenwich, London SE10 9LS, United Kingdom
[b] School of Metallurgy and Materials, College of Engineering and Physical Sciences, University of Birmingham, Edgbaston, Birmingham B15 2TT, United Kingdom

ARTICLE INFO

ABSTRACT

Contactless ultrasound is a novel, easily implemented, technique for the Ultrasonic Treatment (UST) of liquid metals. Instead of using a vibrating sonotrode probe inside the melt, which leads to contamination, we consider a high AC frequency electromagnetic coil placed close to the metal free surface. The coil induces a rapidly changing Lorentz force, which in turn excites sound waves. To reach the necessary pressure amplitude for cavitation with the minimum electrical energy use, it was found necessary to achieve acoustic resonance in the liquid volume, by finely tuning the coil AC supply frequency. The appearance of cavitation was then detected experimentally with an externally placed ultrasonic microphone and confirmed by the reduction in grain size of the solidified metal. To predict the appearance of various resonant modes numerically, the exact dimensions of the melt volume, the holding crucible, surrounding structures and their sound properties are required. As cavitation progresses the speed of sound in the melt changes, which in practice means resonance becomes intermittent. Given the complexity of the situation, two competing numerical models are used to compute the soundfield. A high order time-domain method focusing on a particular forcing frequency and a Helmholtz frequency domain method scanning the full frequency range of the power supply. A good agreement is achieved between the two methods and experiments which means the optimal setup for the process can be predicted with some accuracy.

1. Introduction

The treatment of light alloys in the liquid state with ultrasound has been shown to improve their mechanical properties [1]. This improvement can be attributed to the cavitation of dissolved gases [2,3], with cavitation occurring when the acoustic pressure amplitude exceeds the Blake threshold [4]. Traditional Ultrasonic Treatment (UST) techniques use an oscillating sonotrode probe, immersed in the liquid melt to induce the ultrasound. Contrasting this, the technique shown here uses a contactless electromagnetic sonotrode known as the "Top-Coil" [5,6]. This employs rapidly changing Lorentz forces to induce ultrasonic sound waves into the melt. As the probe is not in contact with the metal it removes the risk of contact contamination and enables use in reactive metals. The ability to water-cool the coil also allows for its use in high temperature alloys. The Lorentz force operating at ultrasonic frequencies, acts in a thin skin layer in the metal in close proximity to the coil. Its amplitude depends on the coil current [7], therefore, to reduce the energy required by the process it is desirable to seek acoustic resonance in the fluid volume being treated. An additional benefit of the contactless ultrasound method is that strong electromagnetic stirring is also induced within the alloy melt [5], spreading the treatment to the full melt volume.

The idea of electromagnetically induced vibrations in liquid metal treatment is not new, in fact Vives [8,9] appears to be the first to suggest this as a possible approach to use in aluminium grain refinement and for that reason he used the combination of a static magnetic field and 50 Hz AC current passing through the melt. He achieved cavitation in a small volume of metal (~0.2 kg) by increasing the static field to 0.7 T and the current to 3500 A. As these values would be impractical for industry, he also suggested the idea of using a resonant cavity to amplify the sound waves generated by the magnetic field. The same combined static field and AC current concept was more recently used by Kaldre et al. [7,10] who applied a steady axial magnetic field (0.5 T) to a small liquid metal zone heated by induction currents (~1000 A at 14.7 kHz). They studied the dispersion of SiC and Pb particles in steel and aluminium melts held in a reduced atmosphere. They identified cavitation using accelerometers attached to the melt container, through the appearance of half harmonics in the sound

spectrum. Although these examples have increased knowledge of the fundamental physics, they are not easily transferable to industry. The requirements for (i) a strong DC magnetic field, (ii) high current and/or (iii) reduced atmosphere to ease gas cavitation, limits their use to laboratory experiments. While the importance of sound waves in the liquid metal is widely recognised (e.g. see [11]), these previous studies did not attempt to map the sound field generated and so did not design for resonance.

In an earlier publication [5] we first introduced the idea of an external AC induction coil, placed close to the melt surface in a crucible, acting as the vibration source. A conical levitation coil was used for this purpose, with its function reversed, i.e. pushing the metal surface downwards by repulsion rather than levitation. This close proximity has the effect of maximising the Electromagnetic (EM) interaction between the coil and the melt. At the same time, we carried out numerical simulations of the resulting magnetohydrodynamic flow, heat transfer and importantly the acoustic waves generated by the time-dependent part of the Lorentz force were presented. However, the sound transmission and reflection through the walls of the crucible were neglected, an omission which is included here.

This prototype 'Top-Coil' shown in Fig. 1, is water cooled with sufficient current running through it to prevent contact with the alloy melt by electromagnetic repulsion. It is also covered by a protective ceramic coating to prevent spark erosion. The coil operates in the range of 6–10 kHz with current amplitudes up to 1700 A. The induced vibrations are then at twice the supply frequency, which is in the ultrasonic range. At this frequency range, current and the induced Lorentz force does not penetrate far into the melt, instead concentrating near the free surface, in the so-called skin layer. The vibrating free surface then acts as a source of sound, transmitting the effect into the bulk of the fluid as ultrasonic pressure waves. This contrasts with the techniques mentioned earlier, that rely on the presence of a static magnetic field to penetrate the full melt volume. In most cases the transmitted sound energy is lower than traditional sonotrode techniques. To reach the necessary pressure levels and coincidentally reduce energy consumption, it is highly desirable for there to be acoustic resonance within the melt and the crucible. This is achieved by critically tuning the power supply frequency depending on factors such as melt volume, crucible (or melt sump) geometry and the sound characteristics of all materials involved. In this contribution we describe the methods used to model the sound field generated by the coil and present aluminium grain refinement results, obtained in a prototype setup under cavitation conditions.

This paper first considers the theory behind contactless ultrasonic cavitation and resonating vessels. It then describes the different numerical models to achieve the results presented, followed by a description of the experimental procedure. Results from both numerical models and experiments are presented and the model is validated against experimental data.

2. Theoretical basis

2.1. Electromagnetic ultrasound generation

The force acting on the liquid aluminium can be represented as a magnetic pressure. This can be derived from the equation for the Lorentz force:

$$\mathbf{F} = \mathbf{J} \times \mathbf{B}, \tag{2.1}$$

where $\mathbf{F}$ is the Lorentz force, $\mathbf{J}$ current density and $\mathbf{B}$ the magnetic field. Combined with Ampere's law

$$\mathbf{J} = \frac{1}{\mu_0} \nabla \times \mathbf{B}, \tag{2.2}$$

where μ_0 is the permeability of free space. This gives

$$\mathbf{F} = \frac{1}{\mu_0}(\nabla \times \mathbf{B}) \times \mathbf{B} = \frac{1}{\mu_0}\left(-\frac{1}{2}(\nabla(\mathbf{B}^2)) + (\mathbf{B}{\cdot}\nabla)\mathbf{B}\right), \tag{2.3}$$

where the magnetic tension, $\frac{(\mathbf{B}{\cdot}\nabla)\mathbf{B}}{\mu_0}$, is a part of the volumetric force. The term $-\frac{1}{2\mu_0}(\nabla(\mathbf{B}^2))$, can be represented as the magnetic pressure, p_m from

$$-\frac{\nabla(\mathbf{B}^2)}{2\mu_0} = \nabla p_m \tag{2.4}$$

where

$$p_m = -\frac{\mathbf{B}^2}{2\mu_0}. \tag{2.5}$$

The time dependent components of this pressure oscillate at double the coil current frequency [5].

2.2. Resonance

To conserve energy and to achieve pressures required for cavitation, it is beneficial to obtain acoustic resonance in the crucible. To obtain accurate resonant modes the sound waves in both the melt and crucible must be modelled. This is due to the similarity in specific characteristic acoustic impedance ($z_0 = \rho c$) for both the alloy melt and the crucible, where z_0 is the acoustic impedance, ρ the mass density and c the speed of sound. As they are similar, the sound is both transmitted and reflected at the crucible wall. The proportion transmitted can be calculated using the equation:

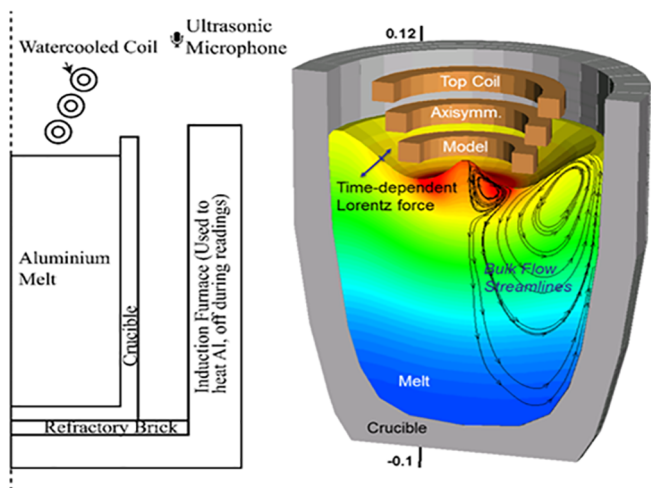$$R = \left(\frac{z_2 - z_1}{z_2 + z_1}\right)^2 \tag{2.6}$$

Fig. 1. (a) Schematic diagram of the "*top-coil*" concept, (b) computed flow, heat transfer and surface deformation, (c) photograph of the experimental setup with the top coil in situ.

where R is the reflected proportion, and z_1 and z_2 the acoustic impedances of the two materials. In seeking resonance the effect of the surrounding container has a significant effect on the resonant modes and must be considered. In contrast, as the difference in acoustic impedance between the crucible and the air is large, it can be assumed that most of sound (i.e. 99.9%) is reflected back into the crucible.

2.3. Cavitation

Cavitation of dissolved gases is considered essential in encouraging nucleation, hence leading to grain refinement in alloys. By seeking the resonant frequencies of the system, pressures greater than the Blake threshold where cavitation may occur can be obtained. The Blake threshold is calculated from

$$P_B = p_0 \left(1 + \sqrt{\frac{4}{27} \frac{S^3}{1 + S}} \right), \quad S = \frac{2\sigma}{R_0 p_0}, \tag{2.7}$$

where p_0 is the ambient pressure, σ the interfacial tension and R_0 the bubble radius [12]. As an example, for bubbles with a radius $R_0 = 5 \times 10^{-6}$ m, an interfacial tension for aluminium and air of $\sigma = 1.1$ N/m and with $p_0 = 101325.0$ Pa gives a Blake threshold of 254 kPa.

Cavitation is seen by industry to have two primary uses in liquid metal processing: the first is degassing, the second that this paper concentrates on, is grain refinement [1]. Grain refinement has been observed in aluminium alloys subjected to UST using conventional immersed sonotrode techniques [13]. There are two primary theories of grain refinement due to cavitation, firstly grain multiplication and secondly cavitation-induced nucleation. The first theory suggests that cavitating bubbles break up solidifying dendrites leading to a larger number of grains [14]. Cavitation-induced nucleation assumes three main mechanisms: (i) non-wettable particles can be transformed into nucleation centres by the melt pressures [15], (ii) the pressure alters the alloy melting [16] and finally, (iii) grain refinement is obtained due to the undercooling of the melt on the bubble surface [16]. In the experiments reported here, the wetting of impurities leading to extra nucleation sites is thought to be the dominant grain refinement mechanism in the contactless sonotrode experiments, as UST is stopped, the samples are removed well above melting temperature and then allowed to solidify.

Since cavitation leads to the emergence of gas bubbles in the liquid, the speed of sound is significantly altered [17]. For driving frequencies much lower than the natural frequencies of the oscillating bubbles and small values of the equilibrium bubble volume fraction β_0, typical for liquid metals, the approximate relation for the effective speed of sound c in the mixture, originally proposed by Wijngaarden [18] can be used:

$$\frac{1}{c^2} = \frac{1}{c_l^2} + \frac{\beta_0 \rho_l}{\gamma p_0} \tag{2.8}$$

where c_l and ρ_l are the speed of sound and density of the pure liquid, γ is the polytropic index of the gas and p_0 is the static pressure. The sensitivity of the effective speed of sound to small changes in the gas bubbles volume fraction is illustrated in Fig. 2.

It can be expected that initially, at the start of the ultrasound treatment and before the cavitation has fully developed, the bubble volume fraction is very low (at the left end of the graph) where the corresponding rate of change is quite mild. With developed cavitation the mean gas volume fraction increases thus changing dramatically the effective speed of sound. This results in resonance being lost (before being regained after a short time) and causes intermittency of the process. With the problems of gas shielding limiting the effectiveness of ultrasonic treatment as reported in immersed sonotrode studies [1] this intermittency is not necessarily undesirable.
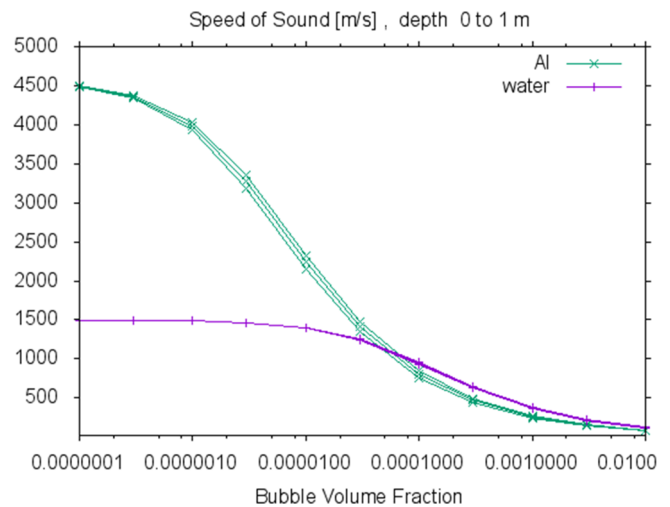

Fig. 2. Speed of sound dependence on gas bubble concentration in liquid aluminium and water computed using Wijngaarden's formula, valid for driving wavelengths much larger than the bubble radius and small gas volume fraction (up to 1e-2). The different lines demonstrate the bubble location, the lowest corresponding to 0 m below surface, the middle 0.5 m below and the top at 1 m.

3. Numerical models

3.1. Time domain acoustic model

As a form of fluid motion, the propagation of sound waves can be described by the equations for mass conservation (3.1) and momentum conservation (3.2).

$$\frac{\partial \rho}{\partial t} + \frac{\partial}{\partial x_j}(\rho v_j) = 0 \tag{3.1}$$

$$\frac{\partial (\rho v_i)}{\partial t} + \frac{\partial}{\partial x_j}(\rho v_j v_i) + \frac{\partial p}{\partial x_i} = F_i; \quad i = 1, 2, 3 \tag{3.2}$$

These are the general forms in Cartesian coordinates x_i with ρ as density, t – time, v_i – the velocity vector components, p – pressure, F_i accounts for both viscous and external forces and the index summation convention is used, e.g. $\frac{\partial v_j}{\partial x_j} = \frac{\partial v_1}{\partial x_1} + \frac{\partial v_2}{\partial x_2} + \frac{\partial v_3}{\partial x_3}$. A relation between pressure and density, needed to close the above system, can be linearised locally as

$$\frac{\partial p}{\partial \rho} = c^2 \tag{3.3}$$

where c is the speed of sound in the medium. Considering liquids where $c \gg v_i$, any terms with a velocity component as a factor may be neglected and the simplified working set of equations (3.4) and (3.5) is obtained.

$$\frac{\partial p}{\partial t} + \rho c^2 \frac{\partial v_j}{\partial x_j} = 0 \tag{3.4}$$

$$\rho \frac{\partial v_i}{\partial t} + \frac{\partial p}{\partial x_i} = F_i; \quad i = 1, 2, 3 \tag{3.5}$$

In sound propagation the viscosity of the medium may be neglected; then, F_i contains the Cartesian components of the electromagnetic force (1.1). The four simultaneous partial differential equations (3.4, 3.5) are solved numerically using a finite difference method optimised for sound propagation [4] that is 4th order accurate in space and 3rd order accurate in time. As the numerical time-stepping scheme is explicit, the size of the time step is subject to a Courant–Friedrichs–Lewy limit which most often is set to 0.2 for the spatial axis with the smallest discretisation step chosen on the basis of a numerical error investigation [19]. In the software implementation used in this work, the two

material properties involved, density and speed of sound, can be spatially varying thus allowing different materials in the geometry set-up. The surface boundary conditions, where liquid or solid are in contact with air, are implemented as zero-acoustic-pressure boundaries due to the negligibly low acoustic impedance of the air.

3.2. Frequency domain acoustic model

For comparison with the time domain simulation an additional model was developed using COMSOL Multiphysics 5.2a. The model is a one way coupled, solving both the driving magnetic field and the acoustic pressures using a Helmholtz equation in the frequency domain. A 2D (axisymmetric) Maxwell model was used for the EM field produced by the coil. This EM field was solved for the entire domain, with a coil approximation for the out of plane coil current density:

$$I_{coil} = \iint \boldsymbol{J} \cdot \boldsymbol{e}_{coil} dr dz, \quad \boldsymbol{J}_e = \sigma \frac{V_{coil}}{2\pi r} \boldsymbol{e}_{coil} \tag{3.6}$$

where I_{coil} is the out of plane coil current, $\boldsymbol{e}_{coil}$ an out of plane unit vector, $\boldsymbol{J}$, the current density in the coil and V_{coil} the voltage in the coil. The boundary conditions are magnetic and electric insulation at the far field boundary.

The magnetic field obtained from the EM solver is used to calculate the magnetic pressure (2.9), this is applied as a background pressure p_b in the melt. The magnetic tension term which is responsible for inducing stirring in the crucible is small compared to the magnetic pressure in this case (by 1 order of magnitude) so for simplicity only the magnetic pressure is used for acoustic simulations:

$$p_b = \frac{\boldsymbol{B}^2}{2\mu_0} \tag{3.7}$$

The pressure acoustics were then solved using the Helmholtz equation in the frequency domain:

$$\nabla \cdot \left(-\frac{1}{\rho_c} (\nabla p_t) \right) - \frac{k_{eq}^2 p_t}{\rho} = 0 \tag{3.8}$$

$$p_t = p + p_b \tag{3.9}$$

$$k_{eq}^2 = \left(\frac{\omega}{c} \right)^2 \tag{3.10}$$

where ρ is the density, p the acoustic pressure, p_t the total acoustic pressure, p_b the background acoustic pressure (defined in (2.7)) ω the angular frequency and c the effective speed of sound in the medium. The background pressure is then applied to the 3D acoustic solver by using the mappings

$$r_{2D} = \sqrt{x_{3D}^2 + (y_{3D} + 0.01)^2}, \tag{3.11}$$

$$z_{2D} = z_{3D}, \tag{3.12}$$

where r_{2D} is the radial coordinate in the 2D model, z_{2D} the z coordinate and x_{3D}, y_{3D} and z_{3D} the coordinates in the 3D model. This has the effect of offsetting the background pressure by 10 mm to obtain asymmetric solutions.

The model uses an unstructured triangular mesh (Fig. 3) refined (0.02–6.7 mm) in the crucible and a much coarser mesh in the surrounding air (0.25–74 mm).

The material properties for both models are outlined in Table 1.

3.3. Cavitation model

When solving for cavitating bubbles, care needs to be taken in choosing numerical algorithms that can handle the near-singular solution which occurs during the rapid implosion of the bubble under intense acoustic pressure oscillations. To model the bubble dynamics, the Keller-Miksis equation [21]

$$\left(1 - \frac{\dot{R}}{C} \right) R\ddot{R} + \frac{3}{2} \dot{R}^2 \left(1 - \frac{\dot{R}}{3c} \right) = \frac{1}{\rho_l} \left(1 + \frac{\dot{R}}{c} + \frac{R}{c} \frac{d}{dt} \right) [p_l - p(t)], \tag{3.13}$$

is chosen which accounts for liquid compressibility and the additional acoustic damping.

The p_l represents the liquid pressure at the liquid gas interface and is defined by

$$p_l = p_g - \frac{2\sigma}{R} - \frac{4\mu\dot{R}}{R}, \tag{3.14}$$

where σ is the surface tension, μ is the liquid viscosity, and p_g is the pressure in the gas at the interface, which can be calculated by using the differential equation

$$\frac{\partial p_g}{\partial t} = \frac{3}{R} \left[(\gamma - 1) \left(k \frac{dT}{dR} \bigg|_{r=R} \right) \gamma p_g \dot{R} \right], \tag{3.15}$$

where γ is the polytropic index, and k the heat conductivity of the gas. The temperature gradient at the bubble surface can be calculated using the method of Toegel et al. [22], which states

$$\frac{dT}{dR} \bigg|_{r=R} = \frac{T - T_\infty}{\sqrt{RD}/3(\gamma - 1)\dot{R}}, \tag{3.16}$$

where D is the gas diffusivity, and T_∞ the bulk temperature of the liquid. The inclusion of acoustic radiation terms is motivated by the significant difference in the response following the explosive collapse of the bubble. The lack of damping in the original Rayleigh-Plesset equation results in overpredicted amplitudes in the oscillation which follows the collapse. For solving the Keller-Miksis equation, a variable-step variable-order Adams-Bashforth-Moulton method [20] is chosen, which has been shown to be particularly efficient in cases where the underlying problem is computationally expensive to solve, or when strict tolerances are needed as is the case here.

Alternatively, an ideal gas law can be used to remove the temperature dependence, resulting in a simpler algebraic solution for the gas pressure. However, due to sharp spikes in temperature when the bubble is undergoing explosive collapse, the ideal gas law does not hold during this phase. The average ambient bubble radius R_0 is often taken to be 5 μm in simulations involving the processing of liquid aluminium [12]. In this model, R_0 is taken to be 4.5 μm to match with Löfsted [23]. The fluid is placed under a 26.5KHz acoustic field with an amplitude of 1.35 atm. All ordinary differential equations in Fig. 8 are solved to a relative tolerance of 1×10^{-13}. Material properties are chosen to match [24] as close as possible, with additional variables for the thermal coupling given by [25]. The difference between the equations is clearly demonstrated in the results which include the effect of acoustic radiation. The equations which lack the term result in much higher amplitudes in the oscillations which follow the bubble collapse. This is in greater agreement with experimental data.

Using the Caflisch equations [26] dissipation functions $\mathscr{A}$ and $\mathscr{B}$ can then be calculated by using the change in void faction over a time period:

$$\mathscr{A} = -\frac{\rho_l \omega^2}{\pi} \int_0^{2\pi} \frac{\partial \beta}{\partial \tau} \sin \tau \, d\tau, \quad \mathscr{B} = -\frac{\rho_l \omega^2}{\pi} \int_0^{2\pi} \frac{\partial \beta}{\partial \tau} \cos \tau d\tau, \tag{3.17}$$

where β is the void fraction and can be calculated using

$$\beta = \frac{4}{3} \pi R^3 N \tag{3.18}$$

where N is the number of bubbles. A full derivation can be found in [19]. If the bubble dynamics are calculated with an equation that does not contain acoustic damping terms, the overpredicted bubble fraction results in dissipation functions (3.18) being inaccurate. These relations can be used in a Helmholtz equation of the form:

$$(\nabla^2 + k^2)p = 0 \tag{3.19}$$

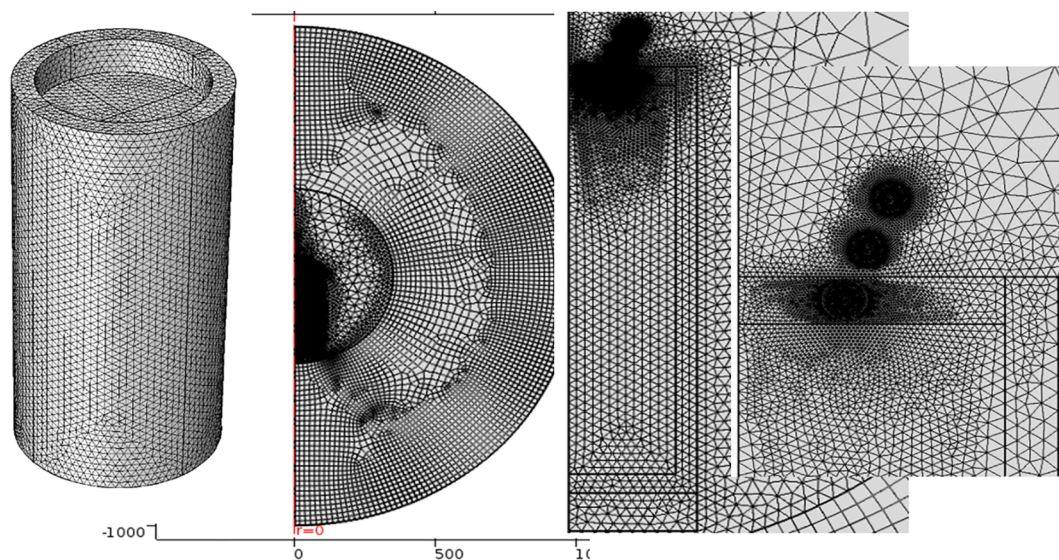where k is a modified wave number and p the pressure:

Fig. 3. Mesh used in the frequency domain model.

$$k^2 = \left(\frac{\omega}{c}\right)^2 - \frac{\mathscr{A}(p)}{|p|} - i\frac{\mathscr{B}(p)}{|p|} \tag{3.20}$$

this equation can be solved in a similar way to the Helmholtz model presented here, noting that the high non-linearity introduced by modifying the wave number makes convergence difficult to achieve.

As the frequency domain solution assumes that the bubble oscillation has a harmonic component, it is important to run the single bubble model for more than one acoustic period so that simulation can converge to a harmonic solution, at which point the dissipation functions $\mathscr{A}$ and $\mathscr{B}$ can be calculated over the last acoustic period.

4. Experimental procedure

About 8.5 kg of commercial purity aluminium (CP-Al) was placed in a cylindrical clay graphite crucible and heated in an induction furnace to about 700 °C. For experiments with a grain refiner about 0.2 wt% of Al-5Ti-1B was added to the CP-Al. The internal and external diameters of the crucible were the same as those of the modeled crucible. To generate ultrasound in the liquid metal, the top-coil was positioned above the liquid metal surface. The frequency around the crucible during the operation was recorded for at least 60 s by an Ultramic200K digital ultrasonic microphone. The recorded data were analysed using MATLAB® software. The recorded sound was observed in the form of a FFT (Fast Fourier transform) sound spectrum in real-time during experiments. When broadband noise was observed, indicating cavitation, the experimental conditions were maintained continuously for 5 min. This period was to bring about any changes due to ultrasound in the melt, and any influence on the microstructure.

Samples for grain refinement tests were taken following the KBI ring test procedure [27]. Liquid metal was poured into a steel ring with an outside diameter of 75 mm, inside diameter 50 mm and height 25 mm, placed on a silica base. The cast sample was subjected to three types of cooling: through the open air, through the steel mould and through the silica brick providing the slow cooling of the sample. The samples were

small (about 50 g), which was beneficial for the top-coil experiment due to previously reported loss of resonance (and grain refinement) due to liquid metal volume change leading to a change in the acoustic modes [28]. Cast samples were prepared for metallographic analysis by removing about 3 mm of the bottom surface of the sample, followed by grinding, polishing, and etching with Poulton's or Keller's solution to reveal the microstructure. The average grain size was determined using the mean line intercept method. These images were taken using a Zeiss Axioskop 2 equipped with AxioCam HRc camera.

5. Results

5.1. Time domain model results

Designing a crucible with suitable resonant frequencies requires three stages: (1) A desired frequency of the power supply is chosen and the driving force is prescribed accordingly. Time-dependent simulations are run for a sufficiently long time to record signals from different locations in the computational domain. For example, 0.1 s real time is sufficient to give a FFT accuracy of 10 Hz. (2) The FFT post-processing then pinpoints possible resonant frequencies in the vicinity of the initially chosen frequency. (3) Shorter simulations driven at the selected resonant frequencies confirm the development of resonance by observing the linear growth in time of the recorded signals. For the examined case with aluminium for which material properties can be seen in Table 1, metal depth 252 mm, inner and outer radii 67.5 and 85 mm, vessel depth 280 mm and outer height 320 mm the 1st and 2nd simulated modes, at the lowest two resonant frequencies, are shown in Fig. 4. The 2nd frequency resonance develops not in the melt, but in the solid base of the crucible, highlighting the risk of crucible breakage during the process.

5.2. Frequency domain model results

The results for a frequency sweep from 18 to 60 kHz at 5 Hz steps in

Table 1
Material properties used in numerical models.

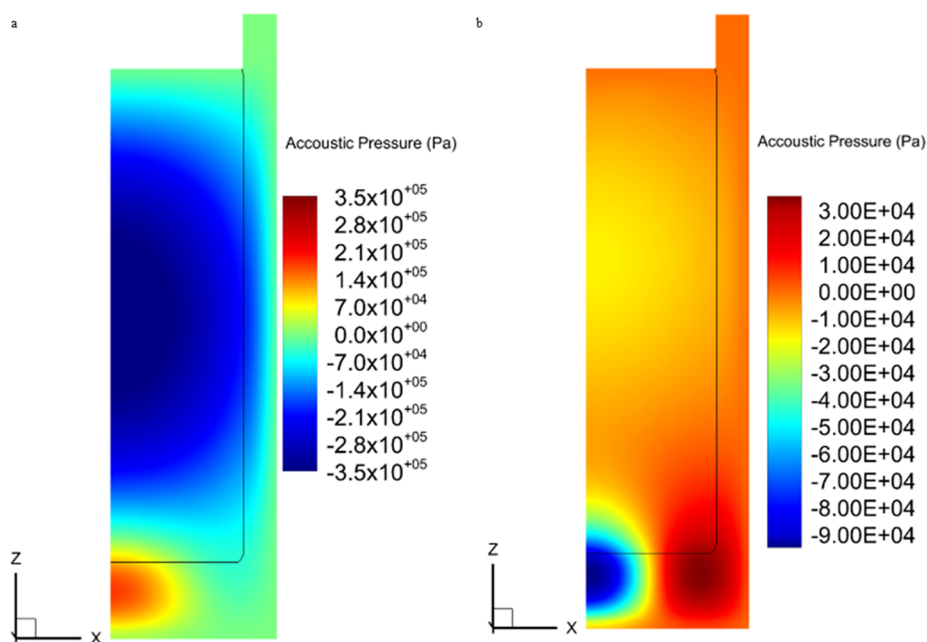| Material	Electrical Conductivity/Sm^{-1}	Mass Density/kgm^{-3}	Speed of Sound/ms^{-1}
Aluminium Melt	2×10^6	2375	4560
Silicon Carbide (crucible)	1×10^5	1844.6	1400
Air	1×10^{-8}	N/A	N/A

Fig. 4. First and second acoustic modes, a) 18470 Hz b) 18956 Hz shown as acoustic field snapshots at the lowest two resonant frequencies, computed using the time domain method.
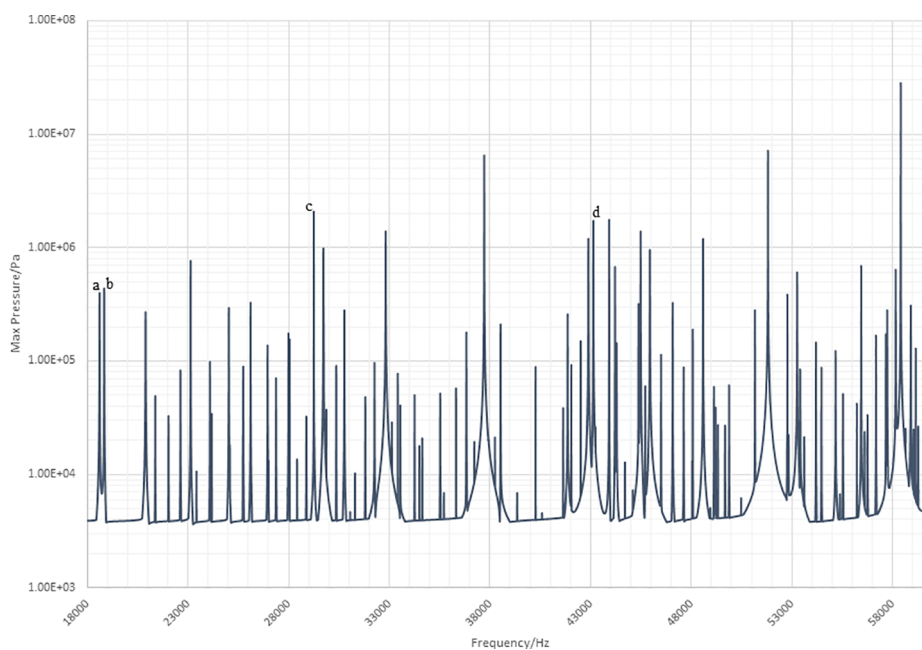

Fig. 5. Maximum pressure in the aluminium melt for 18–60 kHz for the frequency domain model demonstrating the resonant modes (a-d) depicted in Fig. 5. The dominant peaks correspond to 3rd harmonics of the driving frequency, with the dominant value at ~58 kHz.

the Helmholtz model can be seen in Fig. 5. By including the crucible and the aluminium melt a complex pattern of modes forms. The first two modes can be seen in Fig. 6. These modes are also observed in the experimental data. The first is primarily in the aluminium melt and the second in the crucible. The second resonant mode at 18845 Hz could potentially damage the crucible due to the buildup of large forces. Both the time domain model and frequency domain compare favourably, with very similar numerical modes predicted.

Higher frequency modes can also be seen in Fig. 6. These have very complex patterns and contain a larger volume of metal with pressures over the Blake threshold, which may result in an increased cavitation volume. Fig. 7 demonstrates the volumes larger than the Blake threshold, this is the reactive region for cavitation, for the first two

modes. As shown the first mode there is a large region with pressures over the Blake threshold within the melt. The second mode shows that the pressures over the Blake threshold are concentrated around the base of the crucible, this is not ideal for cavitation and may lead to the crucible breaking

5.3. Cavitation model results and speed of sound variation

The Keller-Miksis equation (3.13) has been used to predict the bubble radius variation during cavitation in aluminium. This is compared to experimental data by Löfsted et al. [23] in Fig. 8. As is demonstrated, bubble radii vary from 5×10^{-6} to 5×10^{-5} m. Using equations (3.13) and (3.17) combined with the bubble density N (10^9)
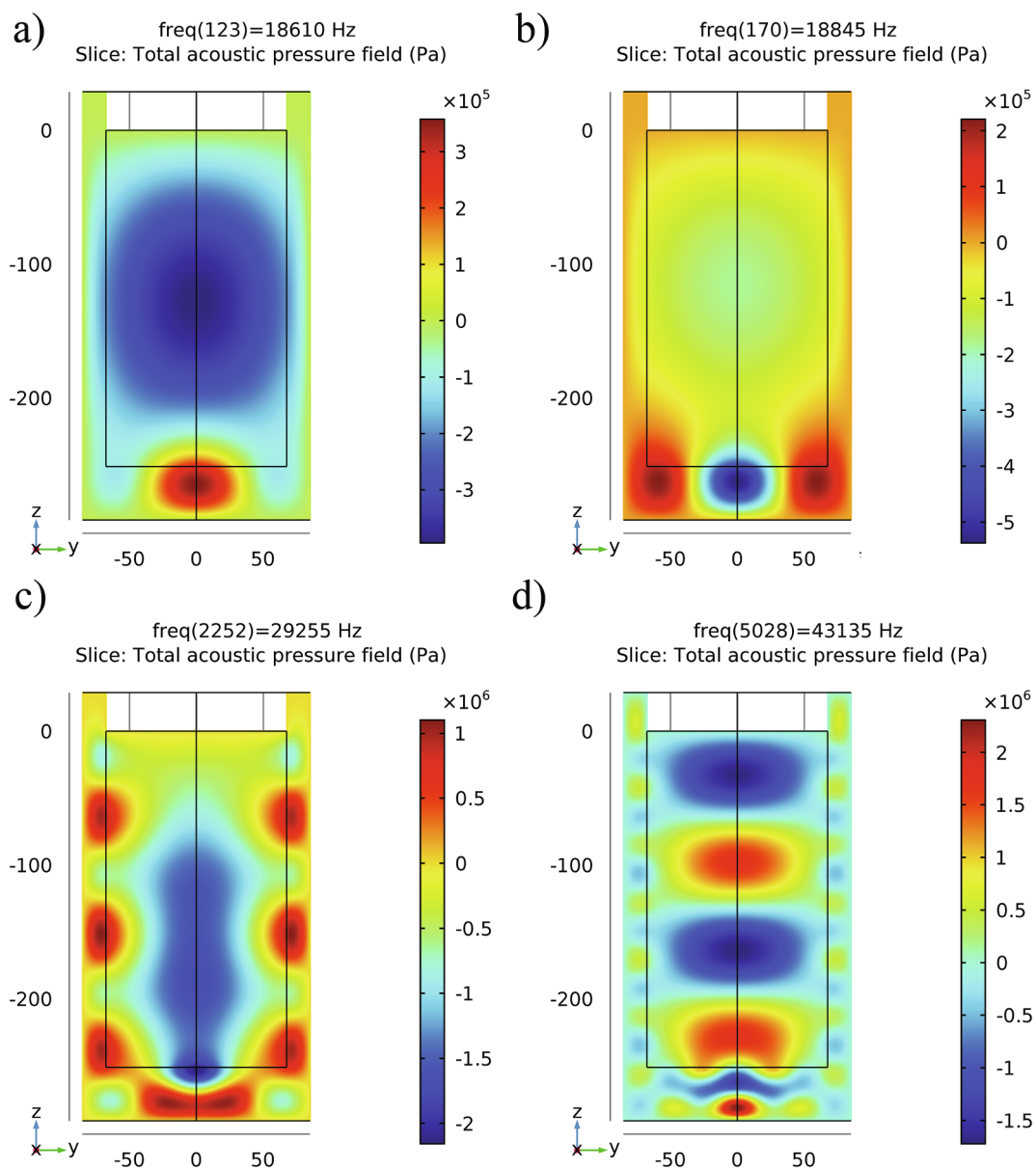
Fig. 6. Frequency domain model pressure plots for high amplitude modes a) 18610 Hz, b) 18845 Hz, c) 29255 Hz and d) 43135 Hz, highlighted in Fig. 4. Note, some of the modes appear inside the crucible material.

and material properties from Lebon et al. [29], an estimate can be made for the speed of sound in areas above the Blake threshold. For an assumed 5 μm bubble radius the speed of sound is reduced from nominal 4560 m/s to 3519.35 m/s and for a 10 μm radius bubble down to 1798.20 m/s.

Using this information an example study was setup with the region above the Blake threshold from the first mode in the frequency domain study at both the speeds of sounds calculated above. This was then run over the range 16–20 kHz in the frequency domain model to demonstrate the shift in the resonant frequencies. These results can be seen in Fig. 9. As shown the resonant frequencies change by 2 kHz for the 3519.35 m/s speed of sound, with the first mode being less than 16 kHz for the 1798.2 m/s speed of sound. This significant change in the speed of sound due to the cavitating bubbles means that resonance is lost due to the bubbles leading to the pulsed nature of cavitation observed in the experimental results.

5.4. Experimental results

The first indication of the presentation of cavitation presence was the observation of broadband noise [6,28], seen as light-coloured lines on the spectrograms recorded under varying conditions. The lines were normal to the continuous horizontal lines denoting the top-coil signal, observed at about 20 kHz and the heating furnace signal, observed at 5 kHz. The frequency of observed broadband noise lines is believed to be a good estimation of the cavitation intensity [6,28]. Recorded sound files are usually 1 min long while the processing time was set to around 5 min and reflects the cavitation intensity (number of cavitation events) during the initial part of processing. The spectral frequency displays for different frequencies are shown in Fig. 10.

Proceeding in steps of ± 20 Hz, it was found that the frequency needed to be tuned to a certain value for any cavitation to appear. Changes in the frequency altered the spectrogram (Fig. 10) and
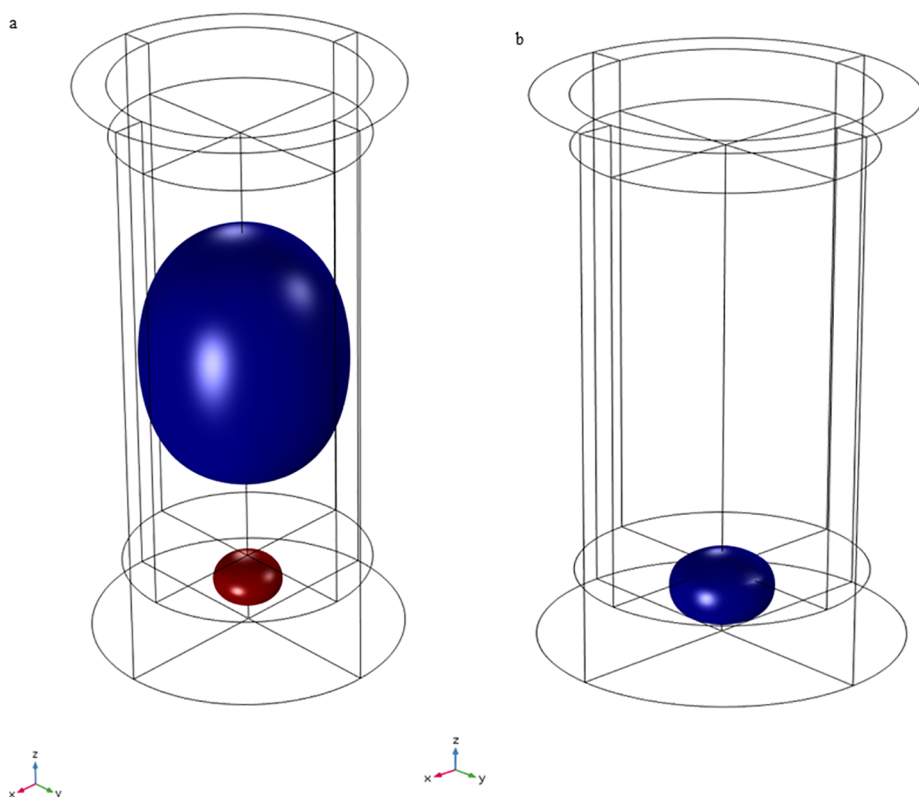
Fig. 7. Blake threshold plots highlighting regions of cavitation activity for the first two modes achievable in the physical experiments, a) 18610 Hz and b) 18845 Hz. The red and blue isosurfaces denote instantaneous in and out of phase modes. (For interpretation of the references to colour in this figure legend, the reader is referred to the web version of this article.)

subsequently grain refinement. For example, at 9.50 kHz, cavitation disappeared (Fig. 10a) but reappeared when the correct resonant frequency was found, at 9.35 kHz (Fig. 10b). The spectrographs (a) and (b) are recorded for almost identical volumes of CP-Al. In the case of Fig. 10, conditions (b) and (c), for CP-AL with the addition of grain refiner were sufficient to bring about microstructural changes. Figs. 11 and 12 show the microstructures of the samples taken during both experiments.

In Fig. 11 the result of grain refinement achieved with CP-Al from 256 μm to 95 μm is demonstrated. The temperature of casting was about 700 °C, 40 degrees above the melting point (the minimum value from the typical pouring range [30]. With higher temperatures the
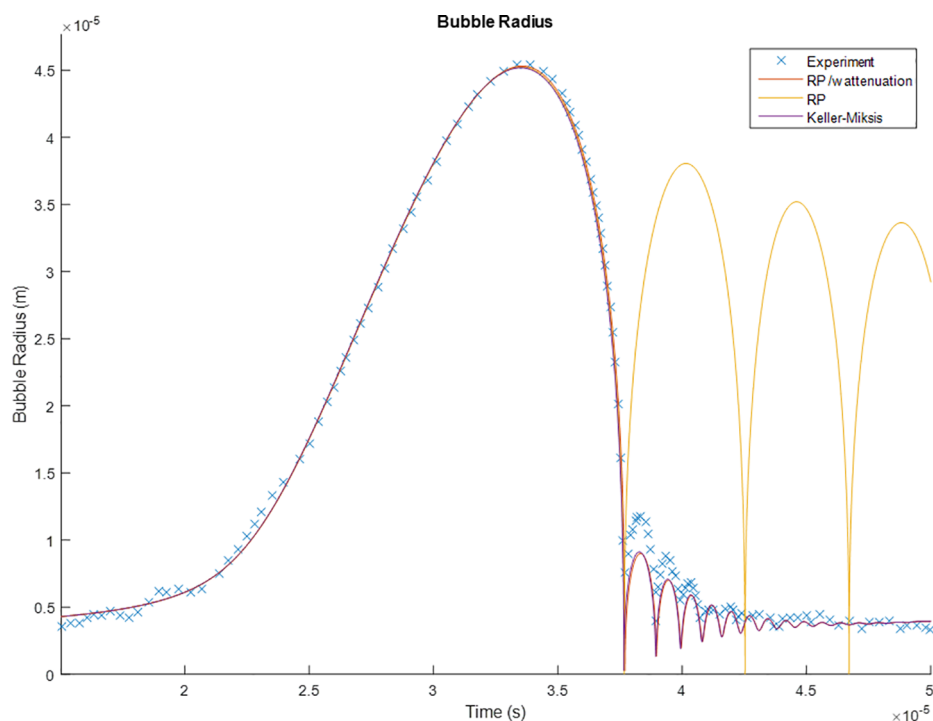

Fig. 8. Bubble collapse, showing a comparison between experimental results by Löfstedt [22], and numerical simulations using Rayleigh-Plesset, a model using Rayleigh Plesset with attenuation and the Keller Miksis equation.
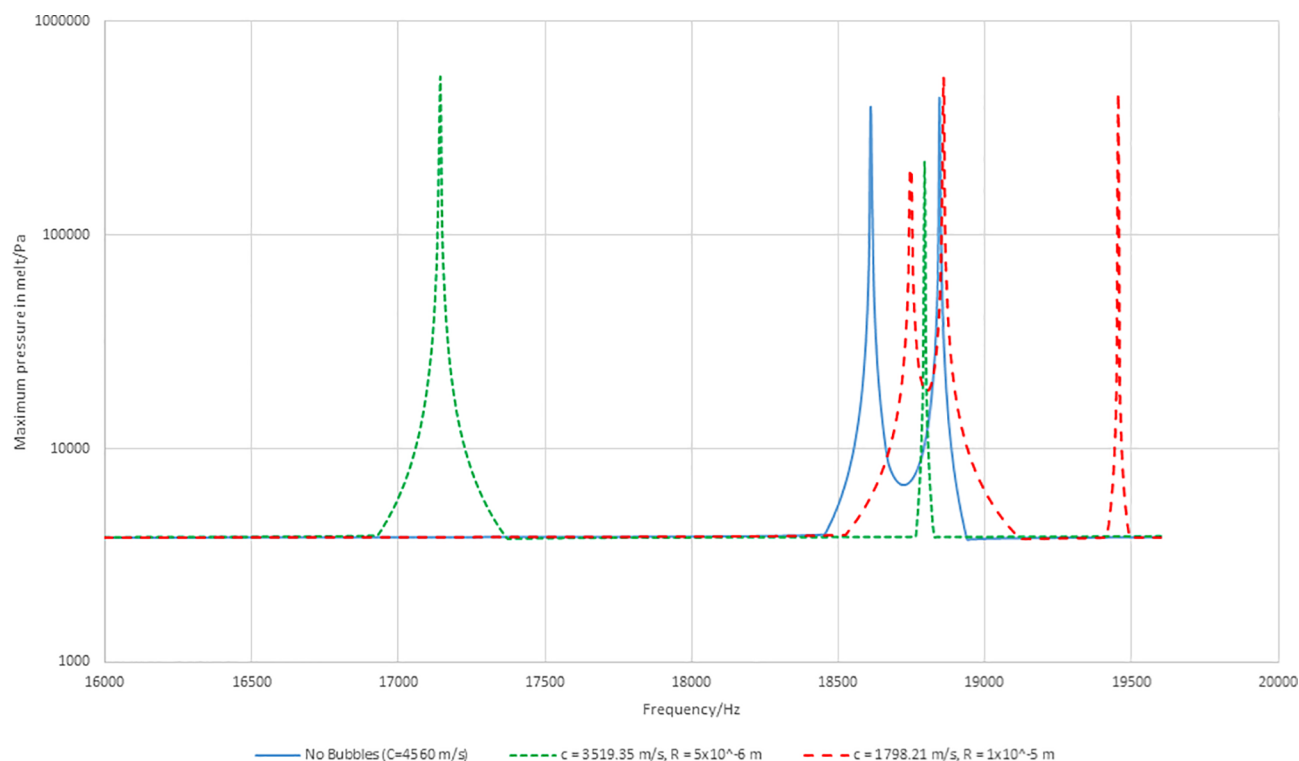
Fig. 9. Graph demonstrating the effect of cavitating bubbles on the resonance in the vessel.
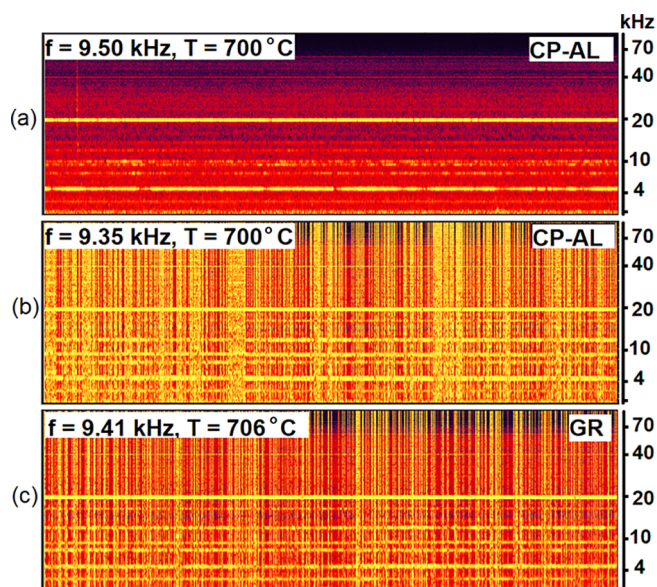

Fig. 10. Spectrograms recorded during experiments: (a) CP-Al absence of cavitation at 9.50 kHz with the continuous horizontal traces due to the top coil forcing frequency at ~20 kHz and the heating coil frequency at ~4 kHz; (b) CP-Al cavitation with broadband noise visible as vertical lines at a chosen *resonant* frequency 9.35 kHz and several harmonics and sub-harmonics appearing as intermittent horizontal traces; (c) similar cavitation broadband noise observed when processing alloy with grain refiner (GR).

amount of cavitation is reduced, this is considered to be due to the gas solubility decreasing with higher temperatures [1,31].

The Al–Ti–B ternary master alloys have been commonly used as grain refiners for most aluminium alloys [32,33]. The mechanism of grain refinement in aluminium due to the addition of Al–Ti–B master alloys, is widely discussed in [32,34,35] but not yet clearly understood [33]. Even if the exact mechanism is not yet established, there are experimental observations of the improved efficiency of the grain refiner effect by the ultrasound processing. The suggested explanation is the deagglomeration and better distribution of the boride particles [36]. The experiments in this case examine whether the effect of the grain refiner can be further improved by processing the alloy with the Top-coil. In Fig. 12, a cross-section of the samples has been presented, revealing the grain sizes in macro-scale. The reduction observed for samples with grain refiner usually varies between 20 and 40%. In the case presented in Fig. 12, the reduction was about 46%, determined from the image of the microstructure, (a reduction from 223 ± 5 μm to 121 ± 2 μm).

The effect of the top-coil measured by grain size reduction was seen in both cases: with commercial purity aluminium and with a CP-AL refined by Al-5Ti-1B. Both broadband noise cavitation lines and resulting grain refinement indicate that cavitation is occurring in the melt. This shows that under correctly tuned conditions this contactless UST can significantly improve the quality of cast metal.

6. Numerical validation

A comparison of the FFT from the experiments, the frequency response results from the scanning Helmholtz model and the FFT of the time domain model can be found in Fig. 13. This shows the results of two experiments with very similar setups. The experimental results showed the two modes close to each other in the 18.5 – 19.5 kHz range. The Numerical results demonstrate the similar double peak in the same range. This suggests that the experimental results are demonstrating the two different peaks as predicted by the numerical model. There is a slight difference (less than 1%) between the predicted frequencies from the numerical models and the frequencies measured in the
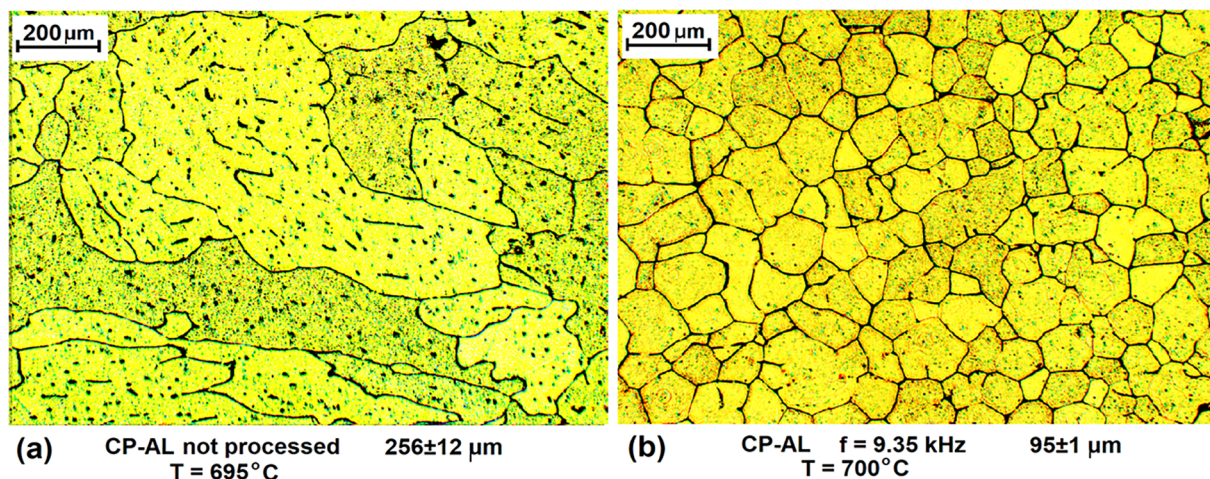
Fig. 11. Grain refinement observed with CP aluminium (a) not processed sample (b) sample processed by the contactless sonotrode with frequency 9.35 kHz. Grain sizes in the processed sample are smaller by ~2.7 times from 256 μm to 95 μm.

Fig. 12. Improvement in the grain refinement using commercial grain refiner. Left, sample refined by the addition of 0.2 wt% Al-5Ti-1B refiner, but no top-coil processing. Right, the alloy additionally processed by the contactless sonotrode at a frequency 9.41 kHz, both samples cast at 706 °C. The grain size reduces from 223 μm to 121 μm.

experimental results. This is likely due to the uncertainty of the speed of sound inside the crucible walls. This sensitivity can be demonstrated, where a change of just 5 m/s in the speed of sound in the crucible results in approximately 50 Hz shift in the observed modes.

Fig. 14 shows the comparison between two numerical models, one assuming sound hard boundaries (Neumann condition) at the edge of the melt, the other modelling the entire crucible. This result does not exhibit the double peak predicted in the full numerical model and observed in the experimental data, highlighting the necessity for the model to include the details of the crucible.

7. Conclusions

Experimental results demonstrate the potential of contactless ultrasonic cavitation for grain refinement in aluminium. Numerical models have been developed to predict the resonant frequencies for the melt prior to cavitation. Comparison with experiments have revealed a good match between the models and experimental data giving insight into the complexities of the resonant system.

Experimentally cavitation has been observed followed by grain refinement after ultrasonic treatment for both LM0 aluminium with and without added grain refiner. The grain refinement in the LM0 is thought to be due to the breaking up and distribution of impurities or remnant microbubbles in the metal resulting in a greater number of nucleation sites. Similarly, grain sizes where reduced in the alloy previously treated with a grain refiner presumably due to a more homogeneous distribution and the breakup of particle agglomerations.

The acoustic models presented here currently predict the initial frequency of the resonant modes. However, this is a dynamic system due to the change in the speed of sound from the cavitating bubbles. Initial attempts to model the change of the speed of sound due to the bubble fraction on the resonant frequencies explain why the cavitation process achieved by the contactless "*top-coil*" device is pulsed and not constant, as resonance is lost when cavitation begins. Future work with the inclusion of the bubble dynamics equations considered earlier in this paper will potentially demonstrate this in a coupled model.
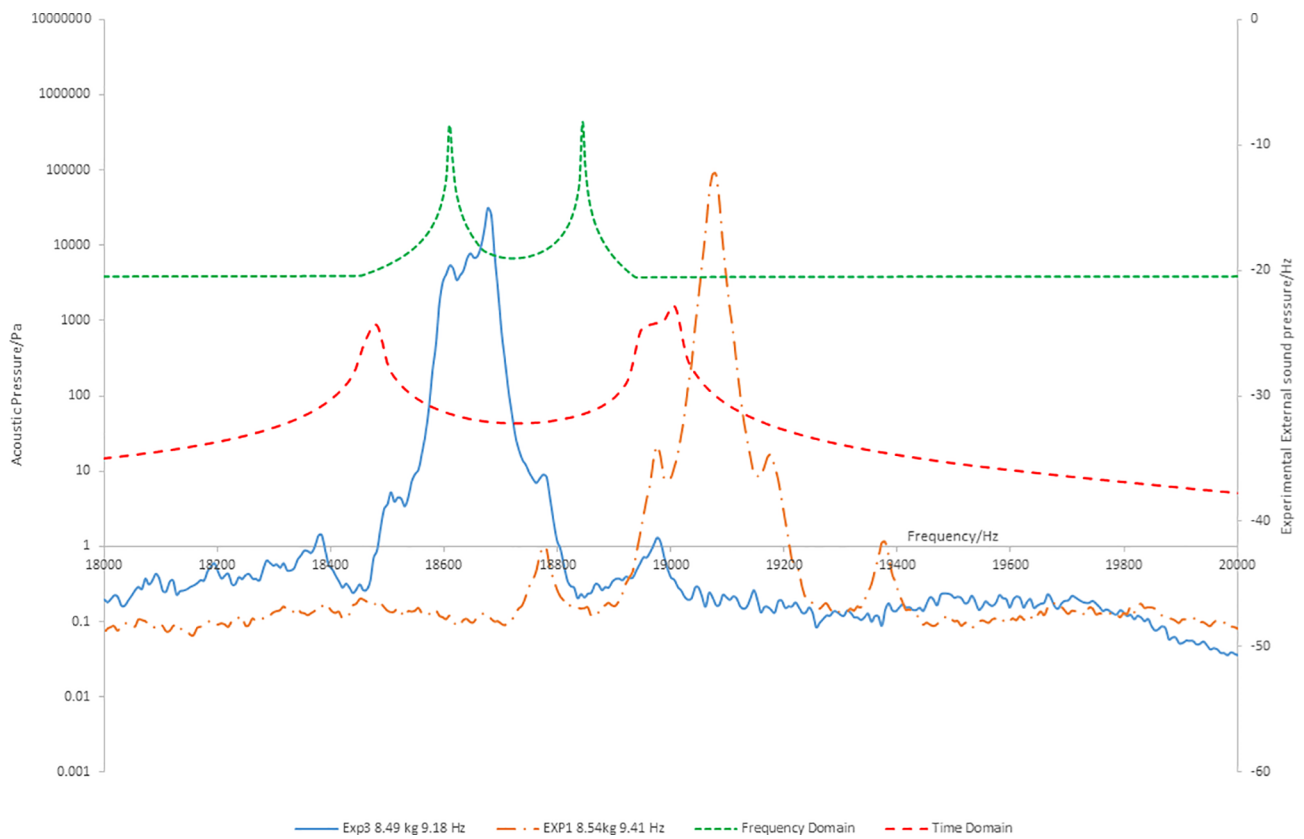
Fig. 13. Comparison of frequency response for the frequency domain model the time domain model and the experimental data. Magnitude for frequency domain and time domain are different as the time domain case is not driven at a resonant frequency but at 19 kHz.
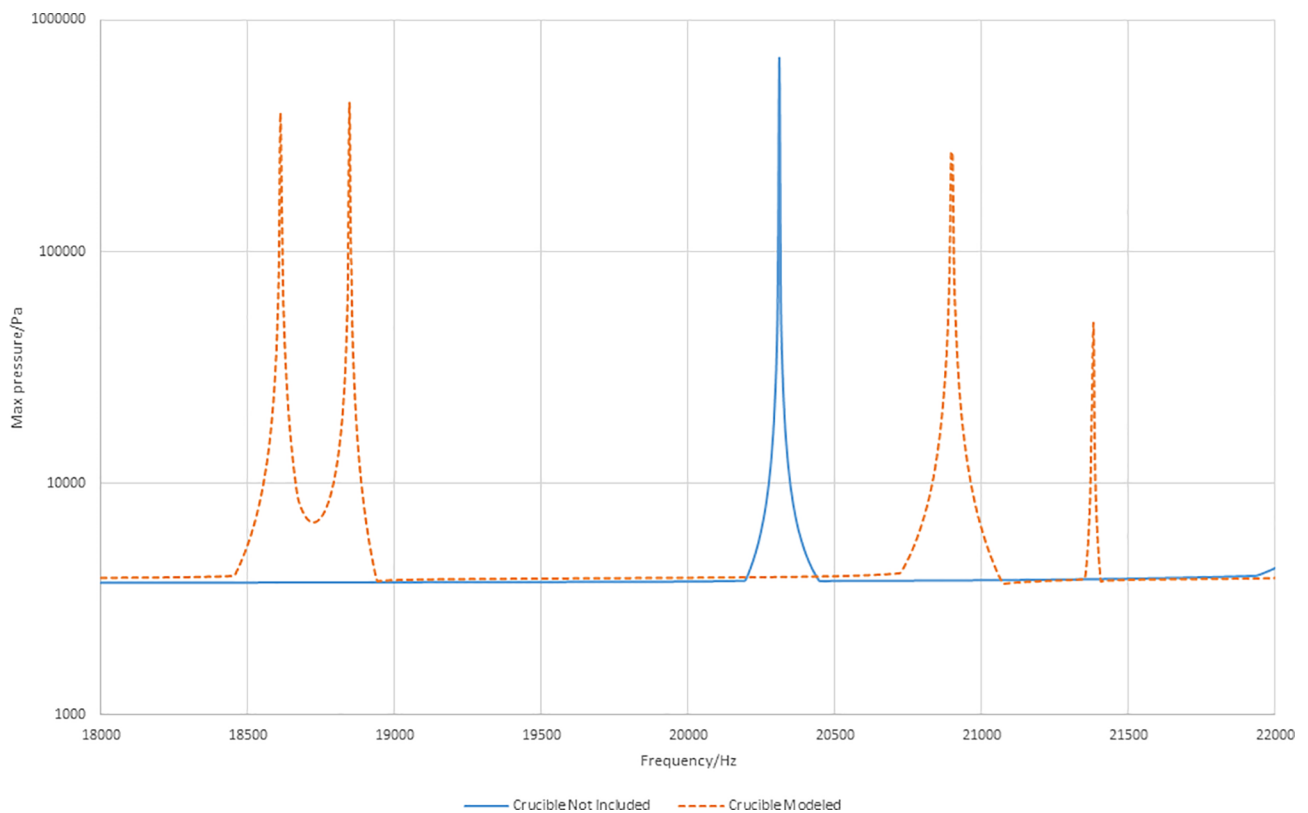

Fig. 14. Comparison of modelling the entire domain including the crucible and excluding the crucible from the numerical model.

Declaration of Competing Interest

The authors declare that they have no known competing financial interests or personal relationships that could have appeared to influence the work reported in this paper.

Acknowledgements

Appendix A. Supplementary data

Supplementary data to this article can be found online at https://doi.org/10.1016/j.ultsonch.2020.104959.

References

[1] G.I. Eskin, D.G. Eskin, Ultrasonic Treatment of Light Alloy Melts, 2nd ed., CRC Press, Boca Raton, 2014.

[2] T. Meek, X. Jian, H. Xu, Q. Han, Ultrasonic Processing of Materials, ORNL/TM-2005/125, 2006.

[3] I. Tzanakis, W.W. Xu, G.S.B. Lebon, D.G. Eskin, K. Pericleous, P.D. Lee, Situ synchrotron radiography and spectrum analysis of transient cavitation bubbles in molten aluminium alloy, Phys. Procedia 70 (2015) 841–845.

[4] G.S.B. Lebon, I. Tzanakis, G. Djambazov, K. Pericleous, D.G. Eskin, Numerical modelling of ultrasonic waves in a bubbly Newtonian liquid using a high-order acoustic cavitation model, Ultrason. Sonochem. 37 (2017) 660–668.

[5] V. Bojarevics, G. Djambazov, K.A. Pericleous, Contactless ultrasound generation in a crucible, Metall. Mater. Trans. A 46A (2015) 2884–2892, https://doi.org/10.1007/s11661-015-2824-5.

[6] A. Manoylov, G.S.B. Lebon, G. Djambazov, K. Pericleous, Coupling of acoustic cavitation with DEM-based particle solvers for modeling de-agglomeration of particle clusters in liquid metals, Metall. Mater. Trans. A 48 (11) (2017) 5616–5627.

[7] I. Grants, G. Gerbeth, A. Bojarevics, Contactless magnetic excitation of acoustic cavitation in liquid metals, J. Appl. Phys. 117 (2015) 204901, , https://doi.org/10.1063/1.4921164.

[8] C. Vives, J. Crystal Growth 158 (1–2) (1996) 118–127.

[9] C. Vives, Grain refinement in aluminum alloys by means of electromagnetic vibrations including cavitation phenomena, JOM-e 50 (2) (1998).

[10] I. Kaldre, A. Bojarevics, I. Grants, T. Beinerts, M. Kalvans, M. Milgravis, G. Gerbeth, Nanoparticle dispersion in liquid metals by electromagnetically induced acoustic cavitation, Acta Mater. 118 (2016) 253–259.

[11] S. Amano, K. Iwai, S. Asai, Non-contact generation of compression waves in a liquid metal by imposition of a high frequency magnetic field, ISIJ Int. 37 (10) (1997) 962–966.

[12] G.S.B. Lebon, I. Tzanakis, K. Pericleous, D. Eskin, P.S. Grant, Ultrasonic liquid metal processing: the essential role of cavitation bubbles in controlling acoustic streaming, Ultrason. Sonochem. 55 (2019) 243–255.

[13] T.V. Atamaneko, D.G. Eskin, L. Zhang, L. Katgerman, Criteria of grain refinement induced by ultrasonic melt treatment of aluminum alloys containing Zr and Ti, Metall. Mater. Trans. A 41 (2010) 2056–2066.

[14] O.V. Abramov, Ultrasound in Liquid and Solid Metals, CRC Press, Boca raton, 1994.

[15] T. Tanaka, Methods of Statistical Physics, Cambridge Universtiy Press (2002) 44–46.

[16] O.A. Kapustina, The physical Principles of Ultrasonic Technology, Nauka, 1920, pp. 592–606.

[17] P.S. Wilson, R.A. Roy, An audible demonstration of the speed of sound in bubbly liquids, Am. J. Phys. 76 (2008) 975, https://doi.org/10.1119/1.2907773.

[18] R.E. Caflisch, M.l.J. Miksis, G.C. Papanicolaou, L. Ting, Effective equations for wave propagation in bubbly liquids, J. Fluid Mech. 153 (1985) 259–273.

[19] G. Djambazov, C.H. Lai, K.A. Pericleous, Staggered-mesh computation for aerodynamic sound, AIAA J. 38 (2000) 16–21.

[20] L.F. Shampine, M.K. Gordon. Computer solution of ordinary differential equations: the initial value problem. (1975).

[21] G. Felipe, L. Crum, C. Church, R. Roy, Sonoluminescence and bubble dynamics for a single, stable, cavitation bubble, J. Acoustical Soc. Am. 91 (6) (1992) 3166–3183.

[22] R. Toegel, B. Gompf, R. Pecha, D. Lohse, Does water vapor prevent upscaling sonoluminescence? Phys. Rev. Lett. 85 (15) (2000) 3165.

[23] R. Löfstedt, Toward a hydrodynamic theory of sonoluminescence, Phys. Fluids A: Fluid Dyn. 5 (1993) 2911.

[24] E. Silberman, Sound velocity and attenuation in bubbly mixtures measured in standing wave tubes, J. Acoustical Soc. Am. 29 (8) (1957) 925–933.

[25] J.B. Keller, M. Miksis, Bubble oscillations of large amplitude, J. Acoustical Soc. Am. 68 (2) (1980) 628–633.

[26] F.J. Trujillo, A strict formulation of a nonlinear Helmholtz equation for the propagation of sound in bubbly liquids. part i: theory and validation at low acoustic pressure amplitudes, Ultrason. Sonochem. 47 (2018) 75–98.

[27] B.S. Murty, S.A. Kori, M. Chakraborty, Grain refinement of aluminium and its alloys by heterogeneous nucleation and alloying, Int. Mater. Rev. 47 (1) (2002) 3–29, https://doi.org/10.1179/095066001225001049.

[28] K.A. Pericleous, V. Bojarevics, G. Djambazov, A. Dybalska, W. Griffiths, C. Tonry, The contactless electromagnetic sonotrode, shape casting, in: 7th International Symposium Celebrating Prof. John Campbell's 80th Birthday, (2019) 239-252, doi: 10.1007/978-3-030-06034-3_23.

[29] G.S.B. Lebon, G. Salloum-Abou-Jaoude, D. Eskin, I. Tzanakis, K. Pericleous, P. Jarry, Numerical modelling of acoustic streaming during the ultrasonic melt treatment of direct-chill (DC) casting, Ultrason. Sonochem. 54 (2019) 171–182.

[30] P. Ager, A. Iortsor, G.M. Obotu, Behavior of aluminum alloy castings under different pouring temperatures and speeds, Discovery 22 (74) (2014) 62–71.

[31] I. Tzanakis, G.S.B. Lebon, D.G. Eskin, K. Pericleous, Investigation of the factors influencing cavitation intensity during the ultrasonic treatment of molten aluminium, Mater. Des. 90 (2016) 979–983.

[32] M.A. Easton, D.H. St. John, A model of grain refinement incorporating alloy constitution and potency of heterogeneous nucleant particles, Acta Mater. 49 (2001) 1867–1878.

[33] A.B. Pattnaik, S. Das, B.B. Jha, N. Prasanth, Effect of Al–5Ti–1B grain refiner on the microstructure, mechanical properties and acoustic emission characteristics of Al5052 aluminium alloy, J. Mater. Res. Technol. 4 (2) (2015) 171–179.

[34] M.A. Easton, D.H. St John, Grain refinement of aluminum alloys: Part I. the nucleant and solute paradigms—a review of the literature, Metall. Mater. Trans. A 30–34 (1999) 1613–1623.

[35] P.S. Mohanty, J.E. Gruzleski, Mechanism of grain refinement of aluminium, Acta Metall. Mater. 43 (1995) 2001–2012.

[36] G. Wang, Q. Wang, M.A. Easton, Role of ultrasonic treatment, inoculation and solute in the grain refinement of commercial purity aluminium, Sci. Rep. 7 (2017) 9729.